

## Research Article

# Particulate Scale Numerical Investigation on the Compaction of TiC-316L Composite Powders

Defeng Wang,<sup>1</sup> Xizhong An ,<sup>1</sup> Peng Han ,<sup>1</sup> Haitao Fu,<sup>1</sup> Xiaohong Yang,<sup>1,2</sup> and Qingchuan Zou<sup>1</sup>

<sup>1</sup>Key Laboratory for Ecological Metallurgy of Multimetallic Mineral of Ministry of Education, School of Metallurgy, Northeastern University, Shenyang 110004, China

<sup>2</sup>Institute of Molecular Medicine, Sechenov First Moscow State Medical University, Moscow 119991, Russia

Correspondence should be addressed to Xizhong An; [anxz@mail.neu.edu.cn](mailto:anxz@mail.neu.edu.cn)

Received 7 June 2019; Accepted 11 November 2019; Published 29 February 2020

Academic Editor: Georgios I. Giannopoulos

Copyright © 2020 Defeng Wang et al. This is an open access article distributed under the Creative Commons Attribution License, which permits unrestricted use, distribution, and reproduction in any medium, provided the original work is properly cited.

This paper presents a numerical investigation on the 2D uniaxial die compaction of TiC-316L stainless steel (abbreviated by 316L) composite powders by the multiparticle finite element method (MPFEM). The effects of TiC-316L particle size ratios, TiC contents, and initial packing structures on the compaction process are systematically characterized and analyzed from macroscale and particulate scale. Numerical results show that different initial packing structures have significant impacts on the densification process of TiC-316L composite powders; a denser initial packing structure with the same composition can improve the compaction densification of TiC-316L composite powders. Smaller size ratio of 316L and TiC particles ( $R_{316L}/R_{TiC} = 1$ ) will help achieve the green compact with higher relative density as the TiC content and compaction pressure are fixed. Meanwhile, increasing TiC content reduces the relative density of the green compact. In the dynamic compaction process, the void filling is mainly completed by particle rearrangement and plastic deformation of 316L particles. Furthermore, the contacted TiC particles will form the force chains impeding the densification process and cause the serious stress concentration within them. Increasing TiC content and  $R_{316L}/R_{TiC}$  can create larger stresses in the compact. The results provide valuable information for the formation of high-quality TiC-316L compacts in PM process.

## 1. Introduction

316L stainless steel (abbreviated by 316L) has increasingly wide utilization in automobile, aerospace, marine, and medical treatment field owing to its outstanding properties of corrosion resistance, ductility, and biocompatibility. However, it is not efficient enough when the strength and wear resistance are both needed [1–3]. The performance of this material can be improved via incorporating hard, brittle ceramic reinforcements into the steel matrix, namely, producing particulate reinforced metal matrix composites (MMCs). Compared with various hard ceramic particles [2–9], titanium carbide (TiC) powder is more suitable and has been widely used as reinforcement in the steel matrix because of its high hardness and strength, high melting point, low density, large elastic modulus, and relative stability [9]. The uniform dispersion of TiC powder within the

316L matrix can result in superior performance of 316L in the application requiring high strength and wear strength. Powder metallurgy (PM) is a promising and economic process to fabricate TiC-316L composites with the advantages of material saving, easy operating, better control of the microstructure, and most importantly net-shape or near net-shape forming [9]. In order to obtain the TiC-316L composites with superior property and investigate the influence of material properties and PM processing parameters on its physical and mechanical performance, a large amount of research work has been carried out.

Initially, people's research interests were mostly focusing on physical experiments. For example, Broeckmann and Schieck [10] studied the failure behavior of 316L composites. Pagounis and Lindroos [4] fabricated 316L composites with different ceramic particulates as reinforcement by hot isostatic pressing (HIP), and the mechanical properties of these

composites were analyzed. They found that a small number of ceramic particles can lead to an improvement in wear resistance, while the tensile strength, ductility, and toughness are reduced. Owing to the key importance of TiC reinforcement in TiC-316L composites, some studies were focusing on the effects of content and size of TiC particles on the physical and mechanical properties of the composites. Khakbiz et al. [11] studied the influence of TiC and different experimental parameters on the rheological behavior of TiC-316L composite powders using powder injection molding (PIM). Lin and Xiong [12] investigated the effects of TiC content and different compaction and sintering methods on the microstructure and mechanical properties of TiC-316L composites. They found that 5 wt.% TiC addition can obtain the densest TiC-316L composites with high mechanical properties. Jin et al. [13, 14] and Onuoha et al. [15, 16] produced TiC-316L composites by cold isostatic pressing (CIP) and melt infiltration sintering. Almangour et al. [17–19] conducted selective laser melting (SLM) process to manufacture TiC-316L nanocomposites, where the influences of the initial TiC particle size, content, and volumetric laser energy on the densification process were analyzed. Aforementioned research work mainly focused on different sintering processes in PM production. Actually, reasonable compaction process can produce high-quality green compact, which can not only simplify or optimize subsequent sintering procedure but also improve the product grade. In recent years, various experiments have been carried out on the compaction of pure copper powder [20, 21], iron powder [20, 22], and Al/ZrO [23] and Al/SiC [24–26] composite powders, which mainly revealed the effects of compaction pressure and processing parameters on the relative density of the compact. On the one hand, for the powder compaction of TiC-316L composite powders, systematic and in-depth studies are less reported; on the other hand, for the particle behavior during compaction, such as particle rearrangement and deformation behavior, force transmission, and stress distribution, along with the densification dynamics and mechanisms, corresponding research studies are sparse in physical experiments due to the difficulties.

Under this circumstance, computer simulations have become effective approaches for analyzing the micro-properties in PM production. One of the most commonly used techniques is the finite element method (FEM) which can provide the particle flow characteristics, relative density, and stress distributions with high computational accuracy and has been successfully applied in our previous studies on the compaction of copper [27] and Fe/Al [28] powders. However, this method is unable to demonstrate the aforementioned particulate scale behavior simply based on the continuum assumptions. In this case, the discrete element method (DEM) can improve the particulate scale understanding of the powder compaction process [29–35], while the effectiveness of DEM numerical simulation is largely limited to small deformation or lower relative density than 0.85 [31]. In recent years, to alleviate the restrictions and difficulties involved in the FEM and DEM modelling, the so-called multiparticle finite element method (MPFEM) has been introduced to comprehensively simulate the

compaction process of various powders such as pure copper [36–38], Al [39], iron [40], composite Fe/Al [41], Al/SiC [42], and other ductile and brittle [43–45] powder mixtures. The advantages of this approach can be attributed to combining the characteristics of FEM and DEM and intuitively presenting the powder movement, large deformation, and stress distribution from the particulate scale, while literature review indicated that to the best of our knowledge, fewer numerical studies have been reported in the compaction of TiC-316L composite powders from particulate scale, and the corresponding densification dynamics and mechanisms during compaction process are still far from fully understood.

In this paper, the MPFEM simulation is conducted to investigate the 2D uniaxial die compaction of TiC-316L composite powders with different initial packing structures. The effects of TiC content (wt.%), size ratio of 316L versus TiC particles ( $R_{316L}/R_{TiC}$ ), and loose and dense initial packing structures on the relationship between relative density and pressure, stress distribution and force transmission, particle rearrangement and deformation, and corresponding densification mechanisms during compaction are systematically characterized and discussed. The obtained highlighted results are meaningful for the forming of TiC-316L composite powder compacts with high quality in PM process.

## 2. Simulation Method and Conditions

The MPFEM simulation of the whole compaction process was performed using commercial software MSC Marc. Different initial packing structures with an assembly of 200 particles were generated by DEM which can effectively reproduce the real die filling process by considering the interparticle forces. Since DEM has been successfully applied in our previous studies on the packing of various spherical and nonspherical particulate systems [46–48] and the heat transfer of spheroids in supercritical water [49, 50], the details of this method are not given here. After generation, the initial packing structure is imported into the FEM model, where each particle is meshed with 132 elements as shown in Figure 1(a). In addition, initial packing structures with different size ratios of 316L versus TiC particles ( $R_{316L}/R_{TiC} = 1, 2, 3, 4, 5$ ) and various TiC contents (TiC% = 0, 2, 5, 10, 15, 20 wt.%) are illustrated in Figures 1(b) and 1(c), where blue and yellow disks, respectively, represent 316L and TiC particles. It needs to specify that, to study the effects of one parameter, other parameters are being fixed. For example, 10 wt.% TiC is fixed to study the particle size ratio effects, and  $R_{316L}/R_{TiC} = 1$  is fixed to study the TiC content effects.

After mesh division, the material properties of TiC and 316L particles, contact interaction, boundary conditions, and mesh adaptability are built and listed in Table 1, where TiC and 316L particles are, respectively, set as elastic and elastic-plastic materials. Meanwhile, individual particles are defined as deformable bodies, while the punches and the die are set as rigid bodies. Displacement boundary condition is applied to the upper punch, and the compaction procedure

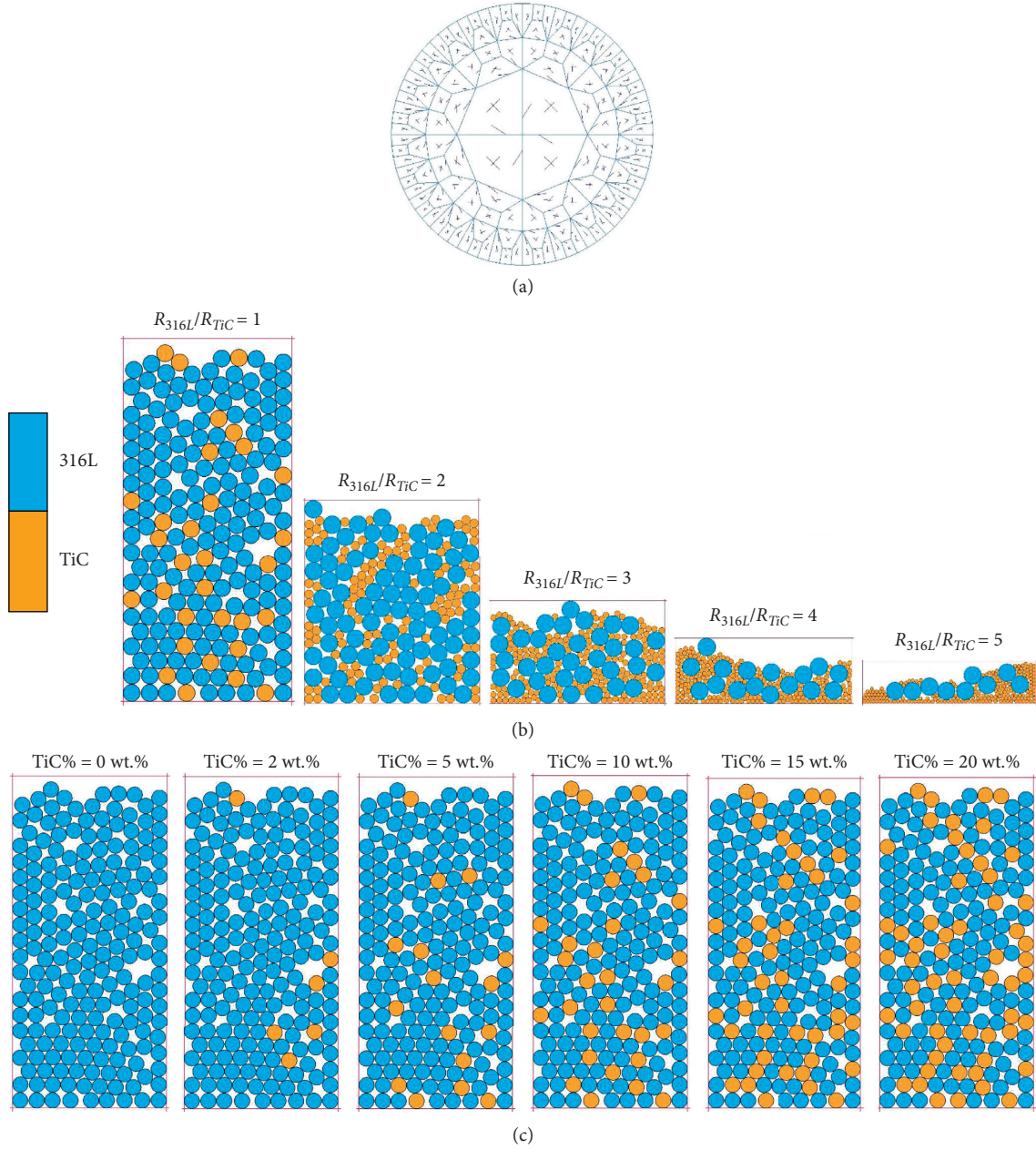


FIGURE 1: (a) Mesh division of the individual particle in the MPFEM model; DEM generated initial packing structures with different particle size ratios (b) and various TiC contents (c).

TABLE 1: Material parameters used for 316L and TiC particles.

Materials	Young's modulus $Y$ , GPa	Poisson's ratio $\nu$ , -	Hardening index $n$ , -	Strength coefficient $C$ , MPa
316L	193	0.29	0.334	273
TiC	440	0.25	—	—

is realized by the downward displacement of the upper punch with the position of the die wall and lower punch being fixed during compaction. In the simulation, the modified Coulomb friction model is adopted, where the friction coefficient  $\mu = 0.2$  is set for particles and  $\mu = 0$  is for the die. Upon compaction, local adaptability and global

remeshing are used to improve the accuracy of the simulation results.

In our MPFEM model, the yield stress can be expressed by [41]

$$\sigma_y = C(\epsilon_0 + \bar{\epsilon})^n + D(\dot{\bar{\epsilon}})^k, \quad (1)$$

where  $\varepsilon_0$  is the initial yield strain;  $\bar{\varepsilon}$  is the equivalent strain;  $\dot{\bar{\varepsilon}}$  is the equivalent strain rate; and parameters  $C$ ,  $D$ ,  $n$ , and  $k$  are material constants. Initially, the equivalent strain and equivalent strain rate are assumed to be zero so that the initial yield strain can be calculated by material constants  $C$ ,  $n$ , and Young's modulus ( $Y$ ) in von Mises material model. The von Mises stress is given by

$$\bar{\sigma} = \frac{[(\sigma_1 - \sigma_2)^2 + (\sigma_2 - \sigma_3)^2 + (\sigma_3 - \sigma_1)^2]^{1/2}}{\sqrt{2}}, \quad (2)$$

where  $\sigma_1$ ,  $\sigma_2$ , and  $\sigma_3$  are the principal Cauchy stresses along three main axes. The equivalent strain rate is

$$\dot{\bar{\varepsilon}} = \left[ \frac{2}{3} (\varepsilon_{ij} \varepsilon_{ij}) \right]^{1/2}, \quad (3)$$

where  $\varepsilon_{ij}$  is the strain tensor.

MSC Marc uses Cauchy stress (true stress) and logarithmic strain with updated Lagrange formulation. It is instructive to derive the stiffness matrices for the updated Lagrangian formulation starting from the virtual work principle as

$$\int_{V_0} S_{ij} E_{ij} dV \delta = \int_{V_0} b_i^0 \delta \eta_i dV + \int_{A_0} t_i^0 \delta \eta_i dA, \quad (4)$$

where  $S_{ij}$  is the second Piola–Kirchhoff stress;  $E_{ij}$  is the Green–Lagrange strain;  $\eta_i$  is the virtual displacement; and  $b_i^0$  and  $t_i^0$  are the body force and the traction vector in the reference configuration, respectively.

### 3. Results and Discussion

**3.1. Macroscopic Property Characterization.** The relationship between relative density  $\rho$  (defined as the volume fraction of the powder in the compact) and compaction pressure  $P$  is firstly established, based on which the influences of 316L and TiC particle size ratio ( $R_{316L}/R_{TiC}$ ), TiC content, and the initial packing structure on the compaction of TiC-316L composite powders are analyzed. Figure 2(a) gives the variations of the  $\rho$ - $P$  curves with different  $R_{316L}/R_{TiC}$  when TiC% = 10 wt.%. It can be seen that three stages can be observed for each case, and the  $\rho$ - $P$  curves show a similar trend, which are in good agreement with those obtained from others' studies [20, 22, 23, 25, 26, 28, 29, 38, 41, 42, 44]. Figure 2(a) also shows that, with the increase of  $R_{316L}/R_{TiC}$ , larger compaction pressure is needed to reach similar relative density. The highest density is achieved when the TiC and 316L particles have the same size, which is in line with the results in the literature [9, 26, 32]. Therefore, the size ratio of the soft and hard powders has distinct influences on the whole compaction process, which needs to be further studied. Meanwhile, the compaction curves of the composite powders with different TiC contents when  $R_{316L}/R_{TiC} = 1$  are shown in Figure 2(b). One can see that the influence of TiC content on the densification is relatively small at the initial stage of compaction with low pressure, and the dominant densification mechanism lies in the particle rearrangement. With the increase of the pressure, the influence of the TiC content becomes significant, which can be ascribed to the

fact that complete deformation of adjacent 316L particles is impeded by the more TiC particles, and the residual pores formed between them cannot be effectively filled. Therefore, with each fixed pressure, the larger the TiC content is, the lower is the relative density of the compact. This phenomenon has been observed during the compaction of other composite powders by different researchers [23, 25, 28, 30, 31, 34, 41, 42, 44]. To validate the current numerical model, Figure 2(c) gives the fitting of the simulation results with Heckel equation [25, 26, 51]:

$$\ln \left[ \frac{1}{(1 - \rho_c)} \right] = MP + A, \quad (5)$$

where  $\rho_c$  is the relative density of the compact;  $P$  is the applied pressure; and  $A$  and  $M$  are constants. Here, the constant  $M$  represents the densification coefficient, which implies that the material with larger  $M$  value can easily achieve higher relative density at a constant pressure. Figure 2(c) illustrates that our simulation results have perfect agreement with the Heckel equation, which demonstrate that the current model is valid and suitable for the particulate scale modelling of TiC-316L composite powders. Furthermore, with the increase of TiC and 316L particle size ratio, the constant  $M$  (the slope of the fitting line) gets smaller, which indicates that the compaction becomes more difficult. Also, the decrease of the slope of the fitting lines with the TiC content demonstrates the poor compressibility when the TiC content is very high.

Meanwhile, the variations of equivalent von Mises stresses with relative density in the TiC-316L composite compacts with different compositions and size ratios during compaction are also analyzed as shown in Figure 3. Here, the equivalent von Mises stresses represent the average value of each node in these compacts. Figure 3(a) indicates that, with the increase of relative density, higher TiC content and larger  $R_{316L}/R_{TiC}$  cause larger equivalent von Mises stresses and more serious stress concentration in the compact. And large stresses shown in Figure 3(b) are mainly concentrated inside TiC particles, which can be ascribed to the fact that plastic deformation of 316L particles can partially release the stresses, but no obvious plastic deformation has been found in TiC particles due to their high Young's modulus. Meanwhile, with the increase of  $R_{316L}/R_{TiC}$ , more voids are formed among the contacting TiC particles due to their large number. These voids are difficult to be fully filled, resulting in a lower relative density of the final compact. In practical fabrication of TiC-316L composites, efforts should be paid in reducing the particle size ratio of composite powders or getting more uniform distribution of reinforced particles to avoid the large local property deviation and get the final compact strengthened. Figure 3 also indicates that the influence of 316L and TiC particle size ratio on the compaction is larger than the TiC content. The prediction of stresses can be beneficial for optimizing the fabrication of high-performance PM components.

In addition, different initial packing structures can also cause distinct densification behavior. Figure 4(a) shows the variations of relative density and equivalent von Mises

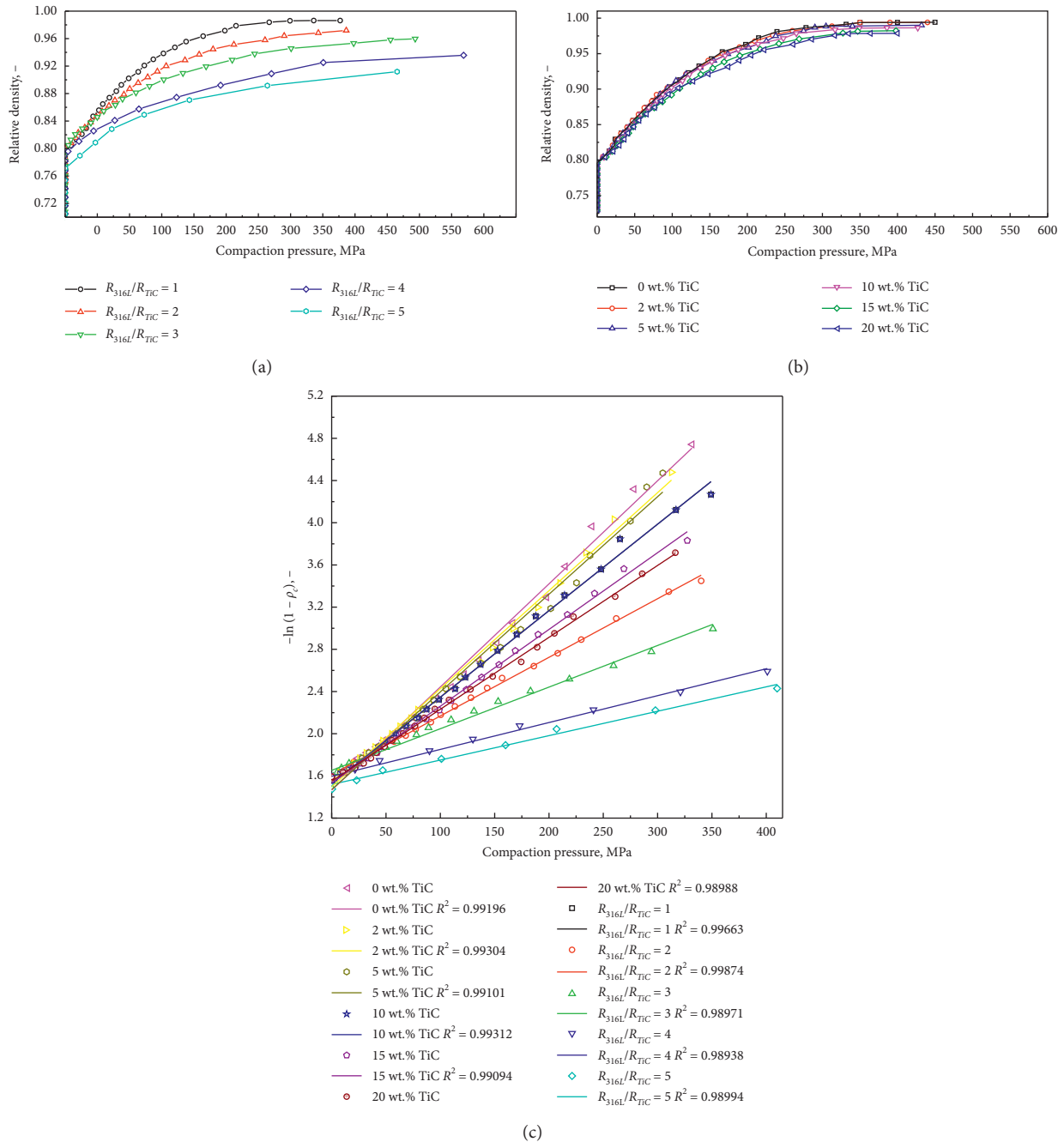


FIGURE 2: Variation of relative density with compaction pressure for TiC-316L composites with (a) different particle size ratios when TiC% = 10 wt.%, (b) various TiC contents when  $R_{316L}/R_{TiC} = 1$ , and (c) fitting of the simulation results in (a) and (b) with Heckel equation.

stresses with compaction pressure of TiC-316L composite powders with the same TiC content (10 wt.%) and particle size ratio ( $R_{316L}/R_{TiC} = 1$ ) but different initial packing structures, and Figure 4(b) gives the morphologies of the two initial packings (with the relative density of 0.7297 for case I and 0.7653 for case II) before compaction and the morphologies after compaction. It is worth mentioning that case II is generated via vibration on case I to obtain a higher initial relative density (tap density). During compaction, the dominant densification mechanism at the initial stage is particle rearrangement [41, 42], where the

mechanical vibration aids the packing densification as can be seen from structure variations in Figure 4(b). From Figure 4, one can also find that the denser initial packing structure (case II) can achieve a higher relative density at the initial stage of compaction. The effect of the initial packing structure on the densification process is more significant at the initial and middle compaction stages; when the relative density reaches a very high value (0.93), the compaction curves of cases I and II tend to be coincided with each other. Even though both cases can reach the same relative density, the compaction pressure in case

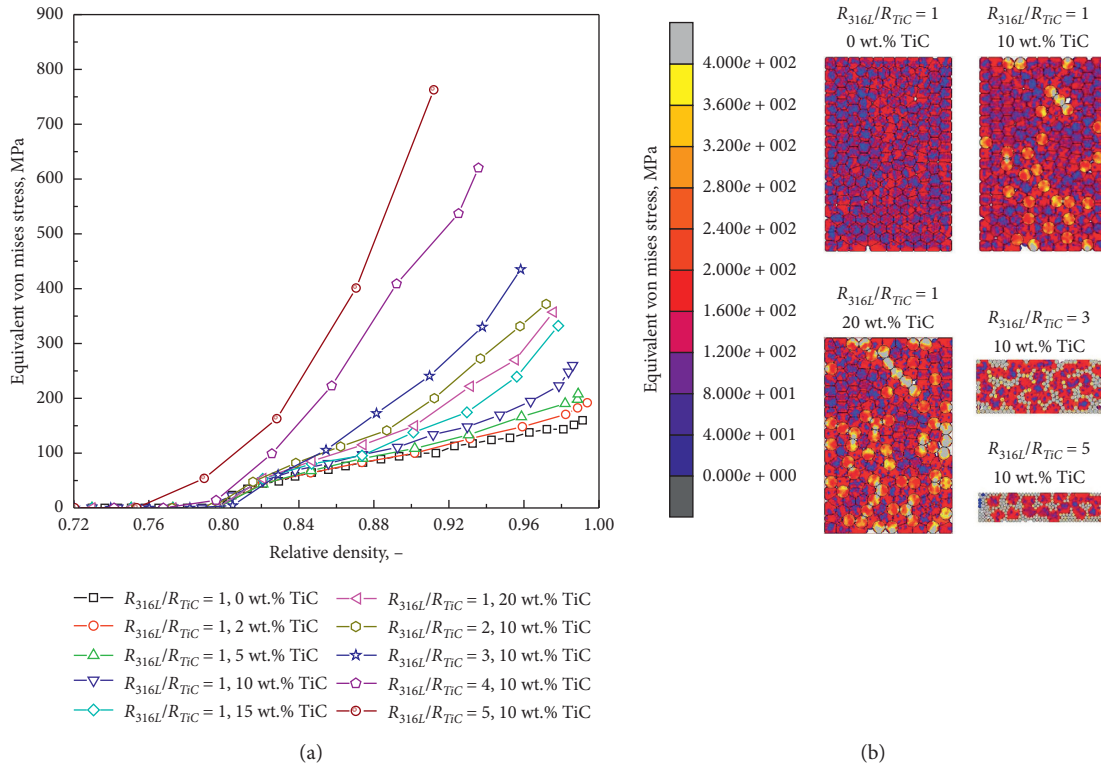


FIGURE 3: (a) Variation of equivalent von Mises stresses with relative density in the compacts during compaction; (b) morphologies of the final compacts with 0 wt.%, 10 wt.%, and 20 wt.% TiC when  $R_{316L}/R_{TiC} = 1$  and 10 wt.% TiC when  $R_{316L}/R_{TiC} = 3$  and 5.

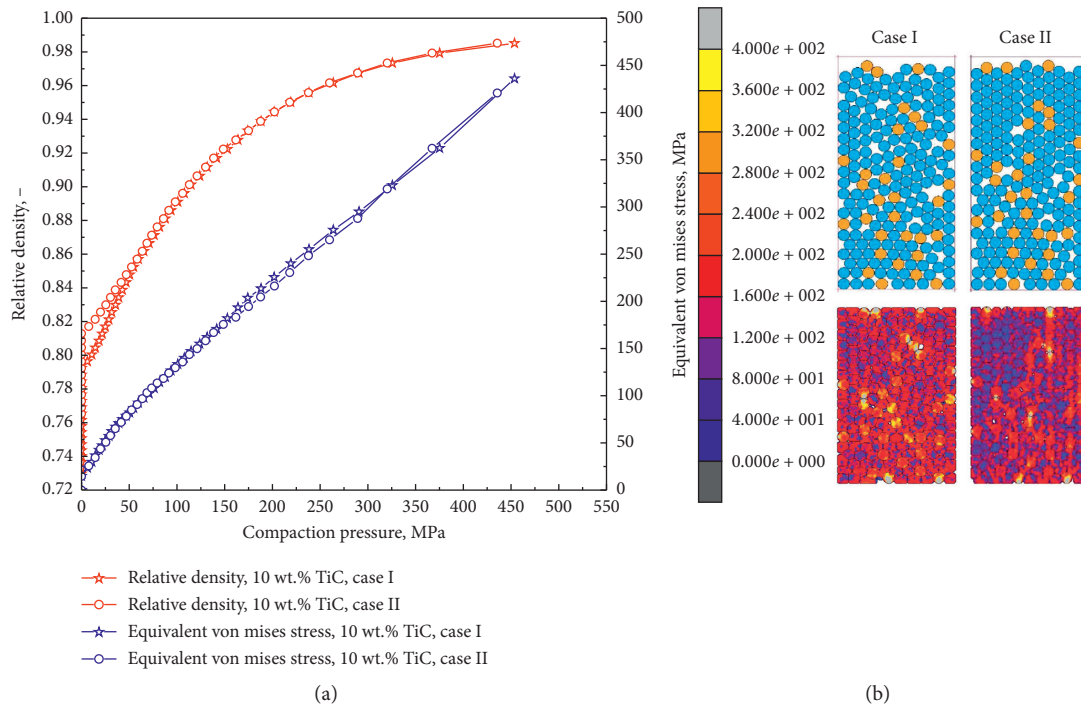


FIGURE 4: (a) Variation of relative density and equivalent von Mises stresses with the pressure during compaction on TiC-316L composite powders with different initial packing structures when TiC% = 10 wt.% and  $R_{316L}/R_{TiC} = 1$ ; (b) morphologies of initial packings with different relative densities (case I:  $\rho = 0.7297$ ; case II:  $\rho = 0.7653$ ) and the morphologies of both final compacts.

II is smaller than that in case I. The simulation results are in good agreement with others' work [42, 44]. In the final compacts, more serious and inhomogeneous stress distributions are identified in case I, which are not beneficial for the subsequent PM process. Meanwhile, fewer large pores are found in the final compact of case II. Therefore, for the compaction of TiC-316L composite powders, a denser initial packing structure can improve the densification process and resultant compact performance.

**3.2. Force Transmission and Densification Mechanism Analysis.** Even the  $\rho$ - $P$  curve can reproduce the relationship between the macroscopic properties of TiC-316L composite powders and the pressure during compaction; it is unable to effectively characterize the particulate scale behavior such as particle rearrangement and deformation and force transmission and densification mechanisms.

To further clarify the densification behavior during compaction, the contact normal force distributions in TiC-316L composite compacts are presented to trace force transmission as shown in Figure 5, where the particle size ratio of 316L and TiC is 1, and the compaction pressure is, respectively, 100 and 300 MPa. The particles with black edges represent TiC powders. From Figure 5(a), one can see that when the compaction pressure is 100 MPa, the force chains formed in these compacts are not distinctly different except that the contact normal forces within TiC particles are larger and more concentrated on the center than the 316L particles at the same position (the TiC particles replace the 316L particles at the same position to achieve the increase of TiC content in the current simulation). As only elastic deformation is occurred on TiC particles, the contact region with its neighbors is not as big as 316L particles, which may induce the contact normal forces nonuniformly transmitted and concentrated within TiC particles. The higher content the TiC is, the more complicated are the force chains formed in the composite compacts, which will further influence the densification behavior of composite powders. When the compaction pressure is up to 300 MPa, the differences of the contact normal force distributions in these composite compacts can be distinctly found in Figure 5(b). With the increase of TiC content, more regions with no contact normal forces are found in the compacts, which indicates that the compaction pressure cannot be effectively transmitted to fulfill the compaction densification, and the local cluster formed by 316L particles will not only hinder the packing densification but also influence the subsequent sintering process due to the nonuniform stress distribution therein. Moreover, the relative densities of the compacts get smaller, and the stress distributions in the compacts become more inhomogeneous. In order to thoroughly and deeply investigate the densification behavior during compaction, the circled areas in Figures 5(a) and 5(b) which are the representative local dense structures are chosen for detailed analysis as given in Figure 6.

Figure 6 gives the local structure evolution in the TiC-316L composite compact during compaction, where TiC % = 20 wt.% and  $R_{316L}/R_{TiC} = 1$ . The marked 6 particles

belong to the TiC powder, and the rest of 10 particles are 316L powder. When the compaction pressure is 50 MPa, the densification is mainly due to the particle rearrangement with the collapse of the "arching" structure. In this case, the relative density of the compact increases sharply. Meanwhile, small deformation of 316L particles can be observed, and the number of contact normal forces within the 316L powder is more than that within the TiC powder, but the value for the former case is smaller than that for the latter case. With the increase of the compaction pressure, one can see that the densification is mainly due to the plastic deformation of 316L particles with more large contact normal forces concentrated within them. It is worth noting that when the compaction pressure is ranging from 100 to 150 MPa, 316L particles have undergone obvious deformation except the one surrounded by TiC particles. This is because compared with 316L particles, the deformation of TiC particles is extremely hard, and the contact region and contact normal forces around TiC particles are also smaller than 316L particles. Therefore, no sufficient pressure is transmitted to the central 316L particle to achieve the plastic deformation; that is to say, the local TiC cluster provides a shelter for the underneath particles and impedes the densification. When the compaction pressure is up to 250 MPa, the deformation extent of the central 316L particle is still smaller than other 316L particles. Even though the addition of TiC particles can improve the performance of the compact, the content of TiC particles should be proper to realize the optimal properties. With the further increase of the compaction pressure (e.g.,  $P > 300$  MPa), the contact normal forces are still larger, but the local structure is nearly stable. The densification is less sensitive with the further increase of  $P$ , which is mainly due to the work hardening of the bulk TiC-316L composite.

Furthermore, Figure 7 shows the contact normal force distributions in TiC-316L composite compacts which have the same TiC content (10 wt.%) but different particle size ratios of 316L and TiC after compaction. One can see that, with the increase of the particle size ratio of 316L and TiC, more contact normal forces are concentrated within the contacting regions of 316L and TiC particles rather than uniform transmission from one particle to another, and the morphologies of 316L particles after compaction are more irregular. Meanwhile, more voids are formed among the contacting TiC particles than those among the contacting 316L and TiC particles. The increasing particle size ratio of 316L and TiC will not only decrease the relative density of the final compact but also aggravate the distribution uniformity of relative density, which is harmful to the mechanical properties of the TiC-316L composites. Therefore, the optimal particle size ratio of 316L and TiC and proper TiC content are of great importance to effectively strengthen the 316L matrix.

**3.3. Quantitative Characterization on Particle Rotation during Compaction.** During compaction, the rotation of particles plays an important role at the initial stage but was generally

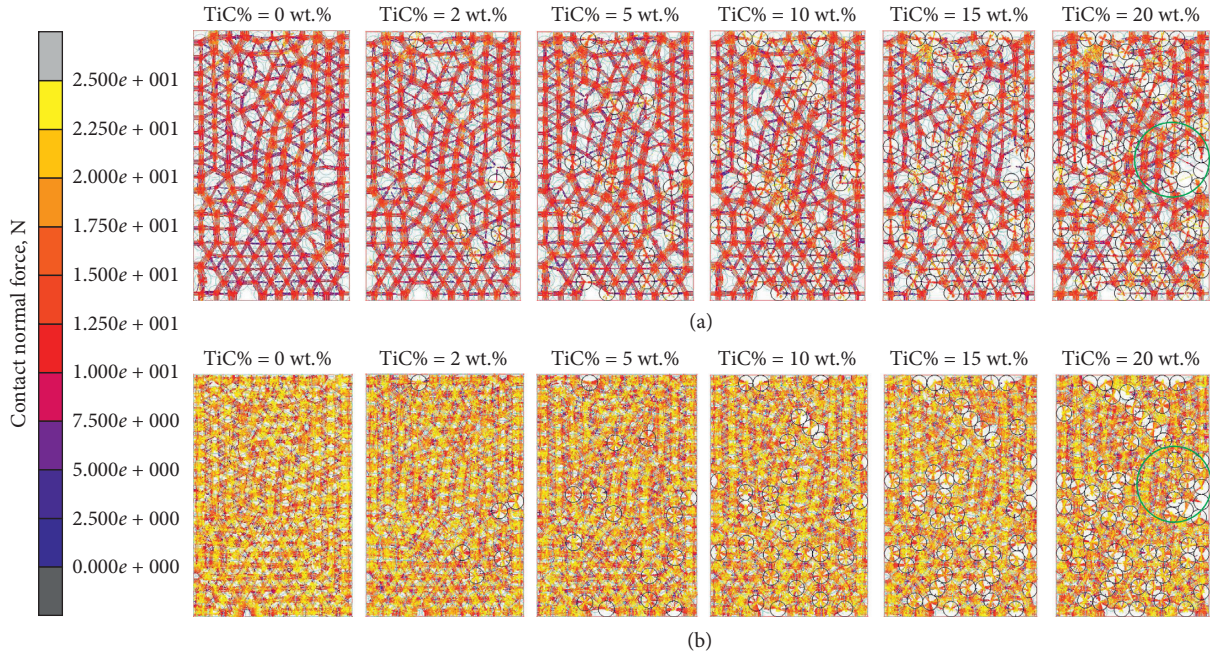


FIGURE 5: Contact normal force distributions in TiC-316L composite compacts with various TiC contents when  $R_{316L}/R_{TiC} = 1$ , where (a)  $P = 100$  MPa and (b)  $P = 300$  MPa.

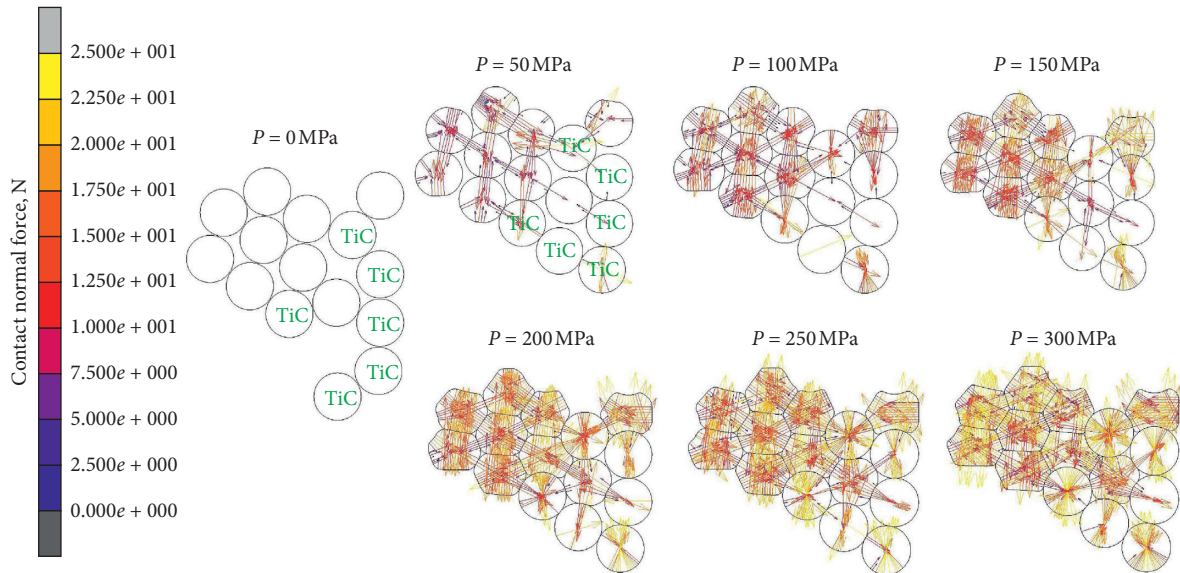


FIGURE 6: Contact normal force distributions of the circled local structure in Figure 5 with TiC% = 20 wt.% when  $R_{316L}/R_{TiC} = 1$  during compaction.

ignored in the analysis of the densification process. Here, a geometric approach is proposed to calculate the degree of particle rotation. The rotation degree is calculated through variation of the particle position from one step to another. Here, the initial coordinates of two nodes (e.g., A and B) located on the circumference of a particle and those (e.g., A' and B') after an incremental step during compaction can be extracted. The following equation is utilized for the calculation:

$$\theta = \arctan\left(\frac{y_2 - y_1}{x_2 - x_1}\right) - \arctan\left(\frac{y'_2 - y'_1}{x'_2 - x'_1}\right), \quad (6)$$

where  $\theta$  is the angle of particle rotation;  $(x_1, y_1)$  and  $(x_2, y_2)$  are, respectively, the initial coordinates of the two nodes A and B; and  $(x'_1, y'_1)$  and  $(x'_2, y'_2)$  are the coordinates of the two nodes A' and B' at the next step. Figure 8(a) gives the relationship between the average value of particle rotation angle and relative density of case I and case II in Figure 4(b)

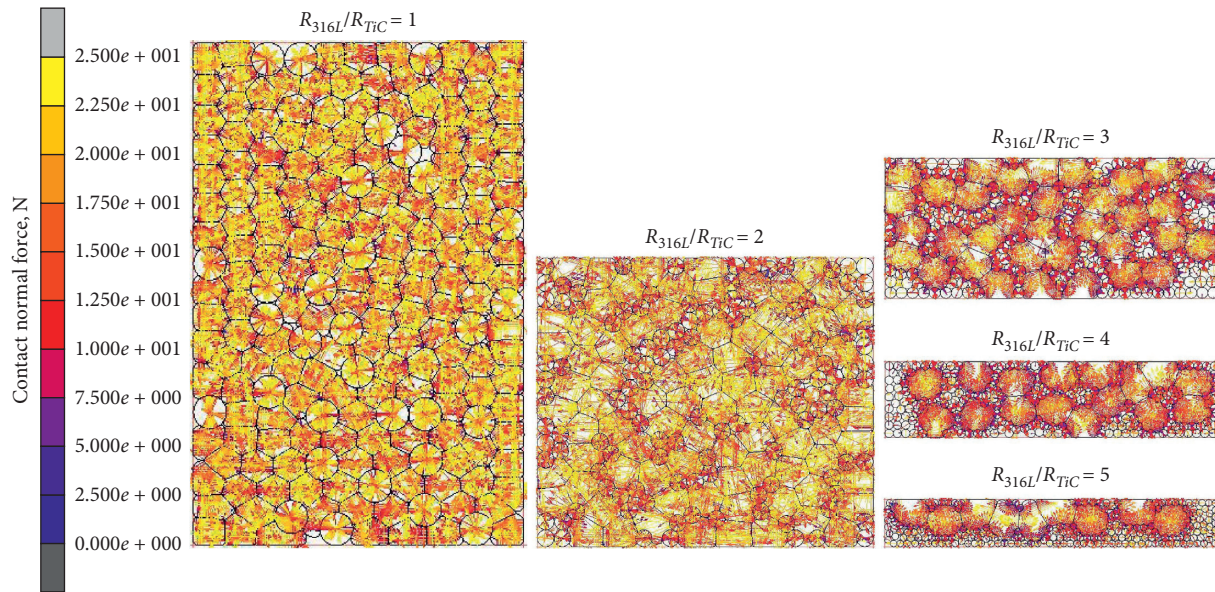


FIGURE 7: Contact normal force distributions in TiC-316L composite compacts with different particle size ratios of 316L and TiC when TiC % = 10 wt.% after compaction.

during compaction. One can see that a similar trend of the curves is observed for both cases, and the average value of particle rotation angle increases with the increase of relative density. When the relative density for both cases is more than 0.82, the particle rotation becomes less sensitive to the further increase of  $\rho$ . This is because 0.82 corresponds to relative density of the random close packing of equal disks in 2D [52] with the jamming state, so the dominant densification mechanism will be transformed to particle deformation when the relative density is beyond this value. As the initial packing structure of case II is more locally ordered and has larger initial relative density than case I, one can find that the average particle rotation of case II is less significant than case I when both TiC-316L compacts reach the same relative density. The frequency distribution of average particle rotation angles is also analyzed and shown in Figure 8(b). For both cases, the average particle rotation angles are mainly concentrated within  $1-5^\circ$ . It needs to be noted that, for case I, the frequency distribution of the particle rotation angle within  $1-5^\circ$  is smaller than that in case II, and the differences between the frequency distributions of other average rotation angles less than  $20^\circ$  are not significant. As the average rotation angles are greater than  $20^\circ$ , the differences of frequency distributions between the two cases are obvious. The frequency of particle rotation angles larger than  $20^\circ$  in case I is higher than that in case II, indicating that the particles in case I rotate with larger angles during compaction to form the final dense structure. In other words, the looser initial structure (case I) needs more “energy” to form a dense compact during the initial stage of compaction. The results show good agreement with the analyses of Figure 4 that the looser initial structure (case I) achieves lower relative density at the initial stage of

compaction. Figure 8(c) gives the contact friction force distributions in the compacts at different compaction stages as marked in Figure 8(a). One can see that the initial stages B1 and B2 have larger relative densities than stages A1 and A2. Here, stages A1 and B1 represent the start of compaction in each case, and stages A2 and B2 represent the starting point of particle rotation as the contact friction force comes into existence. As indicated, the particles in case II can rotate immediately as the compaction starts (no additional increments exist between stages B1 and B2); however, the particles in case I still need to translate to form a more stable and ordered structure for compaction. As the compaction proceeds, the contact friction forces all increase with the relative density of compacts, and the contact friction forces in case I are larger than those in case II. Meanwhile, stages A3, B3 and stages A4, B4 are chosen to analyze the contact friction force distributions due to the same relative density of each case. When the relative density of each case is 0.79635 (A3, B3), as case II has a denser initial structure and the particles are arranged more ordered than case I, the particles in case I need to rotate with larger angle to achieve the same relative density as case II, and the contact friction forces in case I are larger than those in case II. When the relative density of each case is 0.82123 (A4, B4), the structures of both cases transform to the random close packing, and the difference of average particle rotation angle between case I and case II is less significant. At this stage, small deformation starts to appear, and smaller compaction pressure is needed for case II which indicates that the contact friction forces in case II are still smaller than those in case I. Therefore, as discussed above, the denser initial packing structure can aid the packing densification.

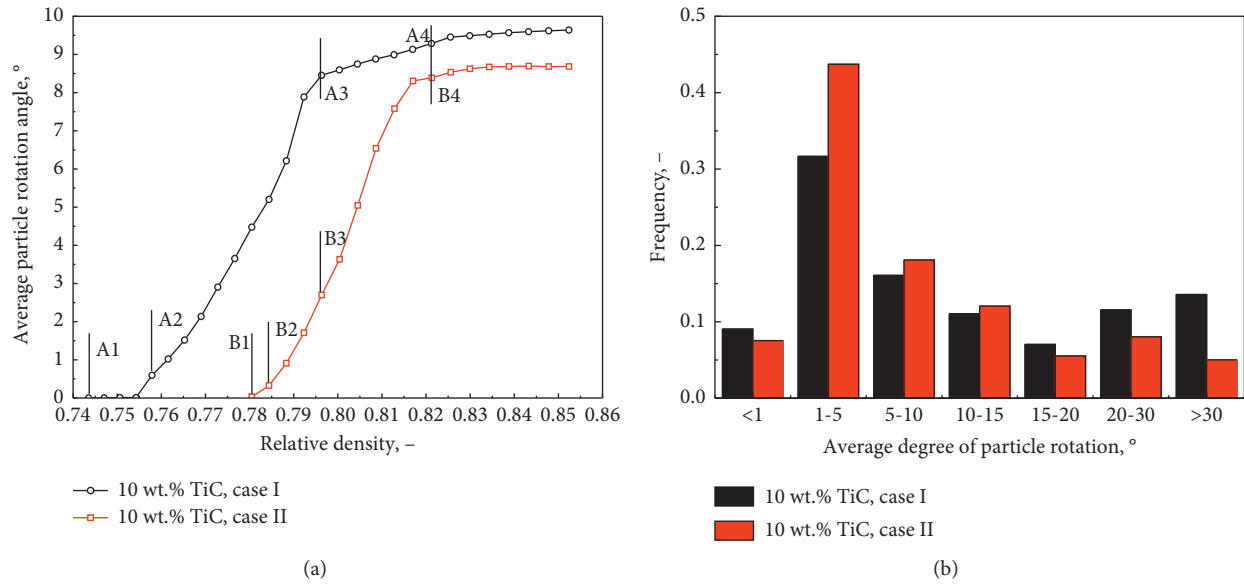


FIGURE 8: Continued.

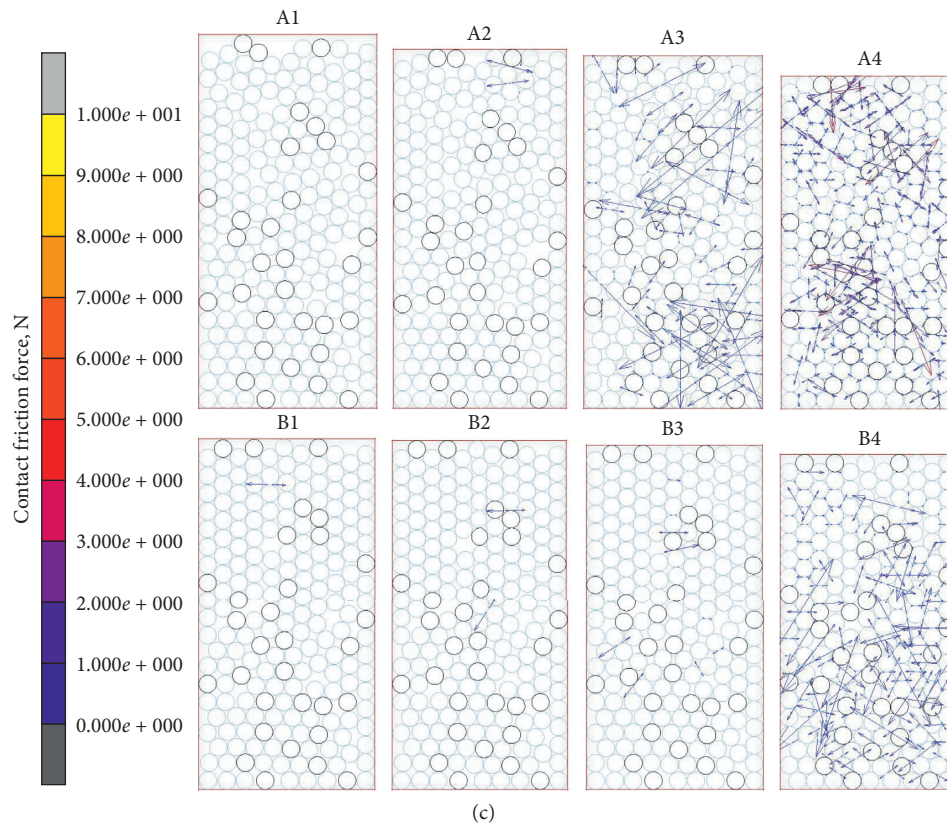


FIGURE 8: (a) Variation of average degree of particle rotation with relative density of cases I and II in Figure 4 during compaction; (b) frequency distribution of average degree of particle rotation in (a); (c) contact friction force distributions of the marked structure in (a) during compaction.

#### 4. Conclusions

Numerical modelling on the uniaxial die compaction of TiC-316L stainless steel composite powders was conducted using the multiparticle finite element method (MPFEM) in 2D. The

effects of TiC-316L particle size ratio, TiC content, and the initial packing structure on the compaction process were investigated. Moreover, macro- and microproperty characterization, particle behavior, and densification mechanism analyses were conducted. The findings are summarized as follows:

- (1) Different particle size ratios of TiC-316L composites ( $R_{316L}/R_{TiC}$ ) and contents of hard TiC particles have significant impacts on the compaction process. When the TiC content and compaction pressure are fixed, the increase of  $R_{316L}/R_{TiC}$  results in the lower relative density and more serious and inhomogeneous stress distribution in the final compact. Similar trend has been observed in the effect of TiC content on the compaction with fixed particle size ratio. If the TiC content is increased in the composite compact, the pressure required for a dense compact increases as well.
- (2) The force chains formed by the network of TiC particles can impede the compaction densification process, which can be ascribed to the stress shielding of underneath particles from deformation for adjacent pore filling. With the increase of  $R_{316L}/R_{TiC}$  and TiC content, more complicated force chains are formed in the compact, and the densification becomes harder.
- (3) At the initial stage of compaction, particle rearrangement, elastic deformation, and small-scale plastic deformation of 316L particles are the dominant densification mechanisms, but their influences on densification are limited. With the increase of compaction pressure, the densification mechanism lies in the large plastic deformation of 316L particles which can effectively fill most of residual pores. Compared with 316L particles, no obvious plastic deformation of TiC particles can be observed due to their high Young's modulus. Therefore, large stresses are mainly concentrated inside TiC particles.
- (4) A denser initial packing structure can improve densification process, and the effects are mainly reflected from the initial stage of compaction as smaller compaction pressure is needed to achieve the same relative density compared with the looser initial packing structure. Meanwhile, the more homogeneous stress distribution in the final compact can also improve the resultant compact performance.
- (5) The contact friction forces in the looser initial structure are larger than those in the denser initial structure in the initial stage of compaction. Particles in initial packing can rotate immediately as the structure becomes much denser and more local ordered at this stage, which indicates that the denser initial packing structure can accelerate the compaction. Moreover, the average particle rotation angle in the denser initial structure is smaller than that in the looser initial structure.

## Data Availability

The data used to support the findings of this study are included within the article.

## Conflicts of Interest

The authors declare that there are no conflicts of interest regarding the publication of this paper.

## Acknowledgments

The authors are grateful to the National Key Development Program of the Ministry of Science and Technology (2017YFB0305603), Liaoning Revitalization Talents Program (XLYC1805007), and Shenyang Young and Middle-aged Science and Technology Innovation Talent Support Program (RC170512) of China for the financial support of the current work.

## References

- [1] F. Laroudie, C. Tassin, and M. Pons, "Hardening of 316L stainless steel by laser surface alloying," *Journal of Materials Science*, vol. 30, no. 14, pp. 3652–3657, 1995.
- [2] J. D. Majumdar, A. Kumar, and L. Li, "Direct laser cladding of SiC dispersed AISI 316L stainless steel," *Tribology International*, vol. 42, no. 5, pp. 750–753, 2009.
- [3] O. Ertugrul, H.-S. Park, K. Onel, and M. Willert-Porada, "Structure and properties of SiC and emery powder reinforced PM 316L matrix composites produced by microwave and conventional sintering," *Powder Metallurgy*, vol. 58, no. 1, pp. 41–50, 2015.
- [4] E. Pagounis and V. K. Lindroos, "Processing and properties of particulate reinforced matrix composites," *Materials Science and Engineering A*, vol. 246, no. 1-2, pp. 221–234, 1998.
- [5] J. Masalski, J. Gluszek, J. Zabrzski, K. Nitsch, and P. Gluszek, "Improvement in corrosion resistance of the 316L stainless steel by means of  $Al_2O_3$  coatings deposited by the sol-gel method," *Thin Solid Films*, vol. 349, no. 1-2, pp. 186–190, 1999.
- [6] S. C. Tjong and K. C. Lau, "Sliding wear of stainless steel matrix composite reinforced with TiB<sub>2</sub> particles," *Materials Letters*, vol. 41, no. 4, pp. 153–158, 1999.
- [7] E. Jajarmi and S. A. Sajjadi, "Fractography of 3YPSZ/316L functionally graded composite subjected to indentation and flexural bending tests," *Ceramics International*, vol. 43, no. 14, pp. 11281–11288, 2017.
- [8] F. T. Cheng, C. T. Kwok, and H. C. Man, "Laser surfacing of S31603 stainless steel with engineering ceramics for cavitation erosion resistance," *Surface and Coatings Technology*, vol. 139, no. 1, pp. 14–24, 2001.
- [9] M. Sheikzadeh and S. Sanjabi, "Structural characterization of stainless steel/TiC nanocomposites produced by high-energy ball-milling method at different milling times," *Materials & Design*, vol. 39, pp. 366–372, 2012.
- [10] C. Broeckmann and A. P. Schieck, "Microstructural aspects of failure in particle reinforced metal matrix composites," *Computational Materials Science*, vol. 5, no. 1-3, pp. 32–44, 1996.
- [11] M. Khakbiz, A. Simchi, and R. Bagheri, "Analysis of the rheological behavior and stability of 316L stainless steel-TiC powder injection molding feedstock," *Materials Science and Engineering A*, vol. 407, no. 1-2, pp. 105–113, 2005.
- [12] S. Lin and W. Xiong, "Microstructure and abrasive behaviors of TiC-316L composites prepared by warm compaction and microwave sintering," *Advanced Powder Technology*, vol. 23, no. 3, pp. 419–425, 2012.

- [13] C. Jin and K. P. Plucknett, "Microstructure instability in TiC-316L stainless steel cermets," *International Journal of Refractory Metals and Hard Materials*, vol. 58, pp. 74–83, 2016.
- [14] C. Jin and K. Plucknett, "The effects of microstructure on Vickers indentation damage in TiC-316L stainless steel cermets," *International Journal of Refractory Metals and Hard Materials*, vol. 61, pp. 151–161, 2016.
- [15] C. C. Onuoha, G. J. Kipouros, Z. N. Farhat, and K. P. Plucknett, "The effects of metal binder content and carbide grain size on the aqueous corrosion behaviour of TiC-316L stainless steel cermets," *International Journal of Refractory Metals and Hard Materials*, vol. 44, pp. 129–141, 2014.
- [16] C. C. Onuoha, C. Jin, Z. N. Farhat, G. J. Kipouros, and K. P. Plucknett, "The effects of TiC grain size and steel binder content on the reciprocating wear behaviour of TiC-316L stainless steel cermets," *Wear*, vol. 350–351, no. 15, pp. 116–129, 2016.
- [17] B. Almagour, D. Grzesiak, and J.-M. Yang, "In situ formation of TiC-particle-reinforced stainless steel matrix nanocomposites during ball milling: feedstock powder preparation for selective laser melting at various energy densities," *Powder Technology*, vol. 326, no. 15, pp. 467–478, 2018.
- [18] B. Almagour, D. Grzesiak, and J. M. Yang, "Selective laser melting of TiC reinforced 316L stainless steel matrix nanocomposites: influence of starting TiC particle size and volume content," *Materials & Design*, vol. 104, no. 15, pp. 141–151, 2016.
- [19] B. Almagour, D. Grzesiak, T. Borkar, and J. M. Yang, "Densification behavior, microstructural evolution, and mechanical properties of TiC/316L stainless steel nanocomposites fabricated by selective laser melting," *Materials & Design*, vol. 138, no. 15, pp. 119–128, 2018.
- [20] X.-K. Sun, S.-J. Chen, J.-Z. Xu, L.-D. Zhen, and K.-T. Kim, "Analysis of cold compaction densification behaviour of metal powders," *Materials Science and Engineering: A*, vol. 267, no. 1, pp. 43–49, 1999.
- [21] X. Z. An, Z. T. Xing, and C. C. Jia, "Cold compaction of copper powders under mechanical vibration and uniaxial compression," *Metallurgical and Materials Transactions A*, vol. 45, no. 4, pp. 2171–2179, 2014.
- [22] C. Zhao, M. K. Jain, M. Bruhis, and R. Lawcock, "An integrated study of die powder fill, transfer and compaction process using digital image correlation method," *Powder Technology*, vol. 208, no. 1, pp. 225–230, 2011.
- [23] K. T. Kim, S. C. Lee, and H. S. Ryu, "Densification behavior of aluminum alloy powder mixed with zirconia powder inclusion under cold compaction," *Materials Science and Engineering A*, vol. 340, no. 1–2, pp. 41–48, 2003.
- [24] I. Sridhar and N. A. Fleck, "Yield behaviour of cold compacted composite powders," *Acta Materialia*, vol. 48, no. 13, pp. 3341–3352, 2000.
- [25] A. H. Tavakoli, A. Simchi, and S. M. Seyed Reihani, "Study of the compaction behavior of composite powders under monotonic and cyclic loading," *Composites Science and Technology*, vol. 65, no. 14, pp. 2094–2104, 2005.
- [26] H. R. Hafizpour, M. Sanjari, and A. Simchi, "Analysis of the effect of reinforcement particles on the compressibility of Al-SiC composite powders using a neural network model," *Materials & Design*, vol. 30, no. 5, pp. 1518–1523, 2009.
- [27] X. Z. An, Y. L. Zhang, Y. X. Zhang, and S. Yang, "Finite element modeling on the compaction of copper powder under different conditions," *Metallurgical and Materials Transactions A*, vol. 46, no. 8, pp. 3744–3752, 2015.
- [28] P. Han, X. Z. An, Y. X. Zhang, and Z. S. Zou, "FEM modeling on the compaction of Fe and Al composite powders," *Journal of Mining and Metallurgy, Section B: Metallurgy*, vol. 51, no. 2, pp. 163–171, 2015.
- [29] E. Olsson and P.-L. Larsson, "A numerical analysis of cold powder compaction based on micromechanical experiments," *Powder Technology*, vol. 243, pp. 71–78, 2013.
- [30] C. L. Martin and D. Bouvard, "Study of the cold compaction of composite powders by the discrete element method," *Acta Materialia*, vol. 51, no. 2, pp. 373–386, 2003.
- [31] C. L. Martin and D. Bouvard, "Isostatic compaction of bimodal powder mixtures and composites," *International Journal of Mechanical Sciences*, vol. 46, no. 6, pp. 907–927, 2004.
- [32] O. Skrinjar and P.-L. Larsson, "Cold compaction of composite powders with size ratio," *Acta Materialia*, vol. 52, no. 7, pp. 1871–1884, 2004.
- [33] E. Mitra, P. J. Hazell, and M. Ashraf, "A discrete element model to predict the pressure-density relationship of blocky and angular ceramic particles under uniaxial compression," *Journal of Materials Science*, vol. 50, no. 23, pp. 7742–7751, 2015.
- [34] D. T. Gethin, R. W. Lewis, and R. S. Ransing, "A discrete deformable element approach for the compaction of powder systems," *Modelling and Simulation in Materials Science and Engineering*, vol. 11, no. 1, pp. 101–114, 2002.
- [35] D. T. Gethin, R. S. Ransing, R. W. Lewis, M. Dutko, and A. J. L. Crook, "Numerical comparison of a deformable discrete element model and an equivalent continuum analysis for the compaction of ductile porous material," *Computers & Structures*, vol. 79, no. 13, pp. 1287–1294, 2001.
- [36] Y. X. Zhang, X. Z. An, and Y. L. Zhang, "Multi-particle FEM modeling on microscopic behavior of 2D particle compaction," *Applied Physics A*, vol. 118, no. 3, pp. 1015–1021, 2015.
- [37] F. Güner, Ö. N. Cora, and H. Sofuoğlu, "Numerical modeling of cold powder compaction using multi particle and continuum media approaches," *Powder Technology*, vol. 271, pp. 238–247, 2015.
- [38] F. Güner, H. Sofuoğlu, and O. N. Cora, "An investigation of contact interactions in powder compaction process through variable friction models," *Tribology International*, vol. 96, pp. 1–10, 2016.
- [39] K. H. Lee, J. M. Lee, and B. M. Kim, "Densification simulation of compacted Al powders using multi-particle finite element method," *Transactions of Nonferrous Metals Society of China*, vol. 19, no. s1, pp. 68–75, 2009.
- [40] G. Gustafsson, H.-Å. Häggblad, and P. Jonsén, "Multi-particle finite element modelling of the compression of iron ore pellets with statistically distributed geometric and material data," *Powder Technology*, vol. 239, pp. 231–238, 2013.
- [41] P. Han, X. Z. An, Y. X. Zhang et al., "Particulate scale MPFEM modeling on compaction of Fe and Al composite powders," *Powder Technology*, vol. 314, no. 1, pp. 69–77, 2017.
- [42] F. Huang, X. Z. An, Y. X. Zhang, and A. B. Yu, "Multi-particle FEM simulation of 2D compaction on binary Al/SiC composite powders," *Powder Technology*, vol. 314, pp. 39–48, 2017.
- [43] A. T. Procopio and A. Zavaliangos, "Simulation of multi-axial compaction of granular media from loose to high relative densities," *Journal of the Mechanics and Physics of Solids*, vol. 53, no. 7, pp. 1523–1551, 2005.
- [44] J. Zhang, "A study of compaction of composite particles by multi-particle finite element method," *Composites Science and Technology*, vol. 69, no. 13, pp. 2048–2053, 2009.

- [45] N. Abdelmoula, B. Harthong, D. Imbault, and P. Dorémus, "A study on the uniqueness of the plastic flow direction for granular assemblies of ductile particles using discrete finite-element simulations," *Journal of the Mechanics and Physics of Solids*, vol. 109, pp. 142–159, 2017.
- [46] X. Z. An, R. Y. Yang, K. J. Dong, R. P. Zou, and A. B. Yu, "Micromechanical simulation and analysis of one-dimensional vibratory sphere packing," *Physical Review Letters*, vol. 95, Article ID 205502, 2005.
- [47] A. B. Yu, X. Z. An, R. P. Zou, R. Y. Yang, and K. Kendall, "Self-assembly of particles for densest packing by mechanical vibration," *Physical Review Letters*, vol. 97, Article ID 265501, 2006.
- [48] B. Zhao, X. Z. An, Y. Wang, Q. Qian, X. H. Yang, and X. D. Sun, "DEM dynamic simulation of tetrahedral particle packing under 3D mechanical vibration," *Powder Technology*, vol. 317, pp. 171–180, 2017.
- [49] H. Zhang, B. Xiong, X. Z. An, C. H. Ke, and G. C. Wei, "Prediction on drag force and heat transfer of spheroids in supercritical water: A PR-DNS study," *Powder Technology*, vol. 342, pp. 99–107, 2019.
- [50] H. Zhang, B. Xiong, X. An, C. Ke, and G. Wei, "Numerical investigation on the effect of the incident angle on momentum and heat transfer of spheroids in supercritical water," *Computers & Fluids*, vol. 179, pp. 533–542, 2019.
- [51] P. J. Denny, "Compaction equations: A comparison of the Heckel and Kawakita equations," *Powder Technology*, vol. 127, no. 2, pp. 162–172, 2002.
- [52] R. M. German, *Particle Packing Characteristics*, Metal Powder Industries Federation, Princeton, NJ, USA, 1989.